



INSTITUT DE FRANCE  
Académie des sciences

# *Comptes Rendus*

---

## *Mécanique*

Tong Zhao Gong, Ahmed Kaci Boukellal, Yun Chen and Jean-Marc Debierre

**Equiaxed growth of interacting Al–Cu dendrites in thin samples: a phase-field study at copper concentrations relevant for practical applications**


Volume 351, Special Issue S2 (2023), p. 233-247

Published online: 13 January 2023

<https://doi.org/10.5802/crmeca.145>

**Part of Special Issue:** Physical Science in Microgravity within the Thematic Group  
Fundamental and Applied Microgravity

**Guest editors:** Olga Budenkova (CNRS, Université Grenoble Alpes, Grenoble INP, SIMaP, 38000 Grenoble, France), Catherine Colin (IMFT, Université de Toulouse, CNRS, INPT, UPS et GDR 2799 Micropesanteur Fondamentale et Appliquée) and Guillaume Legros (ICARE, CNRS UPR 3021, Univ. Orléans et GDR 2799 Micropesanteur Fondamentale et Appliquée)

 This article is licensed under the  
CREATIVE COMMONS ATTRIBUTION 4.0 INTERNATIONAL LICENSE.  
<http://creativecommons.org/licenses/by/4.0/>



*Les Comptes Rendus. Mécanique sont membres du  
Centre Mersenne pour l'édition scientifique ouverte*

[www.centre-mersenne.org](http://www.centre-mersenne.org)

e-ISSN : 1873-7234



---

Physical Science in Microgravity within the Thematic Group Fundamental and Applied Microgravity / *Sciences physiques en microgravité au sein du GDR Micropesanteur Fondamentale et Appliquée*

# Equiaxed growth of interacting Al–Cu dendrites in thin samples: a phase-field study at copper concentrations relevant for practical applications

*Croissance équiaxe de dendrites Al–Cu en interaction dans des échantillons minces: une étude de champ de phase à des concentrations de cuivre pertinentes pour des applications pratiques*

Tong Zhao Gong<sup>® a</sup>, Ahmed Kaci Boukellal<sup>® b</sup>, Yun Chen<sup>® a</sup>  
and Jean-Marc Debierre<sup>® \*, c</sup>

<sup>a</sup> Shenyang National Laboratory for Materials Science, Institute of Metal Research, Chinese Academy of Sciences, Shenyang, Liaoning, 110016, P. R. China

<sup>b</sup> IMDEA Materials Institute, Getafe, Madrid, Spain

<sup>c</sup> Aix-Marseille Université, CNRS, Université de Toulon, IM2NP UMR 7334, 13397 Marseille, France

*E-mails:* tzgong15s@imr.ac.cn (T. Z. Gong), boukellalahmed@gmail.com (A. K. Boukellal), chenyun@imr.ac.cn (Y. Chen), Jean-marc.debierre@im2np.fr (J.-M. Debierre)

**Abstract.** We perform three-dimensional phase-field simulations of equiaxed solidification in Al–Cu thin samples. Purely diffusive conditions are considered in order to describe systems where convection and gravity effects can be neglected. The use of a parallel adaptive finite element algorithm introduced recently [Gong *et al.*, *Comput. Mater. Sci.* **147** (2018) p. 338-352] allows us to reach the domain of copper concentrations used in practical applications ( $c \geq 3$  wt% Cu). We compare the present results with those of a previous study which was restricted to lower copper concentrations ( $c \leq 2$  wt% Cu) [Boukellal *et al.*, *Materialia* **1** (2018) p. 62-69] due to the use of a finite difference code. In the fast dendritic growth regime, our results confirm that the

---

\* Corresponding author.

dimensionless growth length  $\Lambda$  is independent of the copper concentration and the average separation distance between the dendrite nuclei. The new data obtained at higher copper concentrations lead to a more accurate estimate of  $\Lambda$ . Physical arguments are developed to specify the meaning of  $\Lambda$  and the grounds of the scaling law  $\Lambda = \text{cst}$ . Comparisons with available experimental results of the literature give additional support to this scaling law.

**Résumé.** Nous réalisons des simulations de type champ de phase tri-dimensionnel de la solidification equiaxe dans les échantillons minces d'Al-Cu. Des conditions purement diffusives sont considérées pour décrire des systèmes où la convection et la gravité peuvent être négligées. L'utilisation d'un algorithme parallèle adaptatif de type éléments finis proposé récemment [Gong *et al.*, *Comput. Mater. Sci.* **147** (2018) p. 338-352] nous permet d'atteindre le domaine des concentrations en cuivre utilisées dans les applications pratiques ( $c \geq 3$  wt% Cu). Nous comparons nos résultats à ceux d'une étude antérieure qui, en raison de l'utilisation d'un code de différences finies, était restreinte à des concentrations de cuivre plus faibles ( $c \leq 2$  wt% Cu) [Boukellal *et al.*, *Materialia* **1** (2018) p. 62-69]. Dans le régime de croissance dendritique rapide, nos résultats confirment que la longueur de croissance adimensionnée  $\Lambda$  est indépendante de la concentration du cuivre et de la distance moyenne séparant les germes dendritiques. Les nouveaux résultats obtenus aux concentrations plus élevées conduisent à une estimation plus précise de  $\Lambda$ . Des arguments physiques sont développés pour préciser la signification de  $\Lambda$  et les fondements de la loi d'échelle  $\Lambda = \text{cst}$ . La comparaison avec les résultats expérimentaux disponibles dans la littérature scientifique apporte une confirmation supplémentaire de cette loi d'échelle.

**Keywords.** Metals and alloys, Solidification, Solute diffusion, Grain structure, Phase-field, Microgravity.

**Mots-clés.** Métaux et alliages, Solidification, Diffusion des solutés, Structure des grains, Champ de phase, Microgravité.

*Published online: 13 January 2023*

## 1. Introduction

The isotropic physical properties of industrial metallic parts, such as cast engine blocks are usually obtained by using equiaxed solidification processes. Many materials employed in related applications belong to the large family of aluminum alloys [1, 2], like the numerous variants of Al-Cu alloys that have been studied quite intensively over the last decades [3]. Since the final properties of such parts largely depend on the multigrain structure that is formed during their fabrication, predicting and controlling the interactions between two grains that grow toward each other is one of the key points of the equiaxed solidification processes.

Scaling laws that govern the grain growth and the grain-grain interactions in diffusive conditions were recently proposed in reference [4] (hereafter denoted as BEA). These laws are thought to be of practical relevance because they can be extrapolated to predict the dynamics of equiaxed dendrites in materials containing higher copper concentrations  $c_0$ , which are not easy to simulate directly. However, it is still reasonable to question the validity of such extrapolations because it is well known that the selection of the dendrite tip velocity and curvature is affected by the undercooling and thus by  $c_0$  in a nontrivial way [5]. In the present study, phase-field simulations in three dimensions are performed to explore copper concentrations higher than the ones originally used in BEA. This is made possible by implementing the finite element algorithm with an adaptive space mesh introduced in reference [6] (hereafter denoted as GEA).

In the literature about Al-Cu solidification, many of the reported phase-field studies are either for directional solidification [7–9] or for solidification at constant applied undercooling [10]. The case of solidification with a constant cooling rate, as we consider here, is less commonly encountered [4, 11]. In Al-Cu alloys, heat diffuses much faster than mass. Moreover, the latent heat released at the solid-liquid interface of the growing dendrite is easily evacuated through the highly conducting crucible walls [12]. A frozen temperature approximation is thus adopted in the model. The resulting problem is, nonetheless, far from being trivial since the sample temperature is steadily decreased in time, which provokes a drift of the undercooling that drives

solute diffusion. Our model being purely diffusive, is directly suitable to describe experiments in micro-g environments.

In Section 2, we introduce the phase-field model that is used to simulate this process. The constitutive physical equations are discussed together with the corresponding phase-field equations, and their implementation in the numerical code is described. The present numerical results are given in Section 3 and they are used to test growth scaling laws previously obtained in BEA. Physical arguments are developed in Section 4 to justify these scaling laws. Finally, Section 5 summarizes our main conclusions and strategies to compare simulations to experiments performed both on earth and in micro-g conditions are evoked.

## 2. Phase-field model

### 2.1. Physical equations

We consider an aluminum alloy of average copper concentration  $c_0$ . The partition coefficient  $k < 1$  and the liquidus slope  $m < 0$ , so  $m(k-1) > 0$ . At the liquidus temperature  $T = T_0$ , which corresponds to the average alloy concentration, the phase diagram imposes

$$c_0 = (T_0 - T_M) / m, \quad (1)$$

where  $T_M$  is the melting temperature of Al. In the reference frame where the material is at rest, the copper diffusion equation reads

$$\frac{\partial c(\vec{r}, t)}{\partial t} = D \nabla^2 c, \quad (2)$$

where  $c(\vec{r}, t)$  is the copper concentration at location  $\vec{r}$  and time  $t$ , and  $D$  is the solute diffusion coefficient that will be assumed zero in the solid phase (one-sided model). In addition, two local equations must be verified at any interface point. The first one expresses solute conservation and it imposes the interface normal velocity,

$$V_n = -D \left( \frac{\partial c}{\partial r} \right)_\ell, \quad (3)$$

the derivative being taken on the liquid ( $\ell$ ) side, in the direction perpendicular to the solid–liquid interface. The second one is the Gibbs–Thomson equation that expresses local thermodynamic equilibrium and that reads in terms of temperatures,

$$T_i = T_M + mc_i - \frac{\Gamma}{\rho} - \frac{V_n}{\mu}. \quad (4)$$

In this equation,  $\rho$  is the average radius of curvature,  $\mu$  the linear kinetic coefficient, and the Gibbs–Thomson constant  $\Gamma$  is related to the chemical capillary length  $d_0$  through

$$d_0 = \frac{\Gamma}{m(k-1)c_0}. \quad (5)$$

In the present case, solidification results from uniform cooling at a constant rate  $R = 0.5$  K/min. Then the interface temperature  $T_i = T_0 - Rt$ , and we obtain the Gibbs–Thomson equation in terms of concentrations,

$$U_i^* = \frac{c_i - c_0}{(1-k)c_0} = -\frac{d_0}{\rho} - \beta_{\text{kin}} V_n + \frac{Rt}{m(k-1)c_0}, \quad (6)$$

where  $\beta_{\text{kin}} = 1/[m(k-1)c_0\mu]$  is the kinetic coefficient in factor of the interface velocity. In the following, we will use the notation

$$\Theta(t) = -\frac{Rt}{m(k-1)c_0} \quad (7)$$

for the negative undercooling, which decreases in time as a result of the sample cooling.

## 2.2. Phase-field equations

Instead of the usual phase-field  $-1 \leq \varphi \leq 1$ , we use the preconditioned phase-field

$$\psi = \sqrt{2} \tanh^{-1}(\varphi) \quad (8)$$

that was shown to increase numerical precision for a given mesh size [13]. A number of recent phase-field studies confirmed that quantitative results are obtained when using the preconditioned phase-field [4, 6, 14–17]. We adopt the quantitative phase-field model introduced by Karma *et al.* to simulate the solidification of diluted alloys [18, 19]. The evolution equation for  $\psi$  is

$$\begin{aligned} \tau(\vec{n})[1 - (1 - k)\Theta] \frac{\partial \psi}{\partial t} = & W(\vec{n})^2 (\nabla^2 \psi - \sqrt{2} \varphi |\vec{\nabla} \psi|^2) \\ & + \sqrt{2} [\varphi - \lambda(1 - \varphi^2)(U + \Theta)] + \sum_{i=x,y,z} W_0^2 \partial_i \left[ (\vec{\nabla} \psi)^2 a_s \frac{\partial a_s}{\partial (\partial_i \psi)} \right], \end{aligned} \quad (9)$$

where  $\vec{n}$  is the unit vector along the normal to the solid–liquid interface. The anisotropy function  $a_s$  of the interface width,  $W(\vec{n}) = W_0 a_s(\vec{n})$ , is taken to be that of the surface free energy, with  $W_0$  the diffuse interface width. For Al–Cu alloys, the solid–liquid interface is rough at the atomic scale, so the kinetic coefficient  $\beta_{\text{kin}}$  can be set to zero for the low solidification velocities considered here. In practice, this is ensured by imposing two conditions. The first is that the anisotropic relaxation time  $\tau(\vec{n}) = \tau_0 a_s^2(\vec{n})$  and the second that the constant  $\lambda$  that couples the non-dimensional concentration field  $U$  to the phase-field is equal to  $(75/47)D\tau_0/W_0^2$  [20]. Since  $W_0 = \xi d_0$  is adjusted by varying the numerical parameter  $\xi$ , this fixes  $\tau_0 = (47\sqrt{2}/120)(d_0^2/D)\xi^3$ . We follow the usual convention where lengths are scaled by  $W_0$  and times by  $\tau_0$ . The resulting non-dimensional evolution equation for  $\psi$  is then

$$\begin{aligned} a_s^2[1 - (1 - k)\Theta] \frac{\partial \psi}{\partial t} = & a_s^2 (\nabla^2 \psi - \sqrt{2} \varphi |\vec{\nabla} \psi|^2) \\ & + \sqrt{2} [\varphi - \lambda(1 - \varphi^2)(U + \Theta)] + \sum_{i=x,y,z} \partial_i \left[ (\vec{\nabla} \psi)^2 a_s \frac{\partial a_s}{\partial (\partial_i \psi)} \right], \end{aligned} \quad (10)$$

where the crystal cubic anisotropy reads

$$a_s = (1 - 3\epsilon_4) + 4\epsilon_4(n_x^4 + n_y^4 + n_z^4), \quad (11)$$

with  $n_x, n_y, n_z$  are the three components of  $\vec{n}$  and  $\epsilon_4$  the anisotropy strength [21]. As in the case of directional solidification, the imposed undercooling  $\Theta(t)$  is also introduced on the left hand side of this equation to prevent the kinetic coefficient  $\beta_{\text{kin}}$  from deviating in time from its imposed value (zero here) [19]. The non-dimensional concentration field  $U$  is related to the physical concentration field  $c$  through

$$U = \frac{f_U(\varphi)c - c_0}{(1 - k)c_0}, \quad (12)$$

with

$$f_U(\varphi) = \frac{2}{(1 + k) - (1 - k)\varphi}. \quad (13)$$

This is the diffuse interface version of the physical definition given in Equation (6): in the liquid phase,  $\varphi = -1.0$ , so  $f_U(\varphi) = 1.0$ .

As solute diffusion is neglected in the solid (one-sided model), a corrective solute current

$$\vec{j}_{at} = \frac{W_0}{2\sqrt{2}} c_0 (1 - k) [1 + (1 - k)U] \frac{1 - \varphi^2}{\sqrt{2}} \frac{\partial \psi}{\partial t} \vec{n} \quad (14)$$

is introduced in the concentration evolution equation in order to counterbalance the excess of solute trapping and other spurious corrections due to the finite interface thickness  $W_0$  [18, 19]. The non-dimensional evolution equation for  $U$  then reads [6]

$$\begin{aligned} [(1+k) - (1-k)\varphi] \frac{\partial U}{\partial t} = & [1 + (1-k)U] \frac{1-\varphi^2}{\sqrt{2}} \frac{\partial \psi}{\partial t} \\ & + \vec{\nabla} \cdot \{D^* (1-\varphi) \vec{\nabla} U\} \\ & + \vec{\nabla} \cdot \left\{ [1 + (1-k)U] \frac{1-\varphi^2}{2} \frac{\partial \psi}{\partial t} \frac{\vec{\nabla} \psi}{|\vec{\nabla} \psi|} \right\}, \end{aligned} \quad (15)$$

where

$$D^* = \frac{D\tau_0}{W_0^2}. \quad (16)$$

### 2.3. Implementation

In the present work, we very closely follow the numerical implementation described in GEA. The finite element method, together with parallel computing with multiple processors using distributed memory based on MPI protocol, is employed to solve the phase-field (PF) equations (10) and (15). The code is developed based on the open source package of deal.II (Differential Equations Analysis Library) [22]. For PF simulations, a sufficiently fine mesh is necessary to get quantitative results but this usually leads to very low computing efficiency when  $c_0$  is increased. Since the PF varies steeply across the interface but remains constant in the bulk solid and liquid phases, an adaptive mesh refinement/coarsening algorithm is thus preferable to accelerate the calculations. With this mesh adaptation we obtain a non-uniform computational mesh with refined elements in the interface layer while grid elements are coarser in the bulk phases. As a result, the number of grid points automatically increases during the dendrite growth. The dimensionless minimum grid size in the interface layer is set to  $(\Delta x)_{\min} = 0.78$ , and the maximum grid size in the bulk liquid and solid phases  $(\Delta x)_{\max} = 8(\Delta x)_{\min}$ . Time is discretised using the implicit Euler method with the dimensionless time step  $\Delta t/\tau_0 = 0.1$ . More detailed information about this procedure can be found in the documentation of deal.II [23] and our previous work [6].

The advantage of using GEA algorithm is evidenced in Figure 1, where the number of grid points in the adaptive mesh is estimated at time when the tip velocity reaches a maximum and is compared with the the finite difference method used in BEA, where a uniform mesh was adopted. Obviously, using the adaptive mesh results in a substantial drop in the grid points number. The grid number gain is already 2 times for a two percent copper concentration but it greatly increases at higher concentrations because the number of mesh points continues to increase as the cube of copper concentration in the finite-difference code, while it slowly decreases in the adaptive mesh code. This is the reason why simulations at copper concentrations higher than 2 percent were not considered in [4]. In addition, the grid refinement algorithm we use does not pose serious overhead problems since the computing time required for grid refinement takes a very small proportion of the total calculation time (less than five percent) [24]. Comparisons of the numerical results obtained by both algorithms were made for  $c_0 = 2$  wt% Cu. As seen below (for instance in Figures 4 and 6), we obtained very similar results from the two codes. This confirmed that the two implementations are compatible and are very likely to be free of numerical artifacts.

The main physical parameters of the Al–Cu alloys are listed in Table 1. For the partition coefficient  $k$  and the liquidus slope  $m$ , we use the average values  $k = 0.14$  and  $m = -2.6$  K/wt% Cu taken from [25]. Closer looks at the phase diagrams of diluted alloys indicate that the liquidus and solidus lines are usually curved, even at small solute concentrations  $c_0$  [26]. However, as shown recently, taking into account the variations of  $k$  and  $m$  with  $c_0$  does not significantly affect

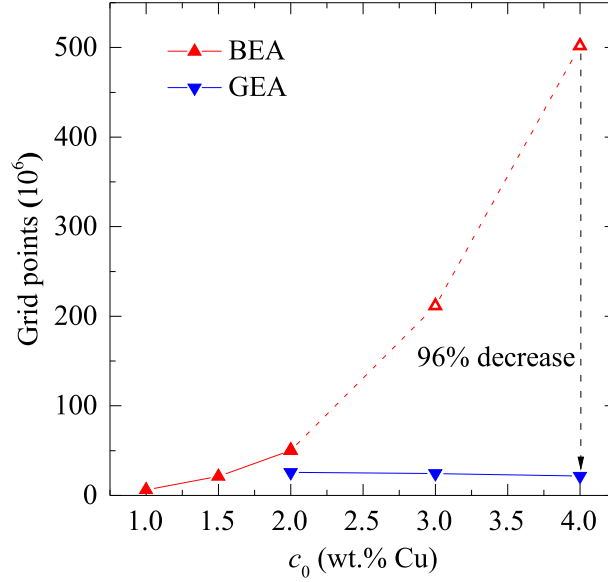


**Figure 1.** Comparison at the maximum tip velocity  $V = V_m$  of the number of grid points in the 3D PF simulations between BEA using uniform mesh and a finite difference scheme and GEA using adaptive mesh and a finite element scheme.  $L = 1000 \mu\text{m}$ . The dotted portion of the BEA curve is extrapolated from the size of the numerical domains used with  $c_0 \leq 2$  wt% Cu. The reduction factor in grid points of GEA compared with BEA is 49%, 86% and 96%, respectively for  $c_0 = 2, 3$ , and 4 wt% Cu.

**Table 1.** Physical parameters of the Al–Cu alloys considered in the simulations.

Symbol	Physical parameter	Value	Unit
$D$	Copper diffusion coefficient in the liquid	3000.0	$\mu\text{m}^2/\text{s}$
$T_M$	Aluminum melting temperature	933.0	K
$c_p$	Aluminum specific heat at melting temperature	$2.8 \times 10^{-12}$	$\text{J}/\text{K}/\mu\text{m}^3$
$c_0$	Copper concentration	1.0–4.0	wt% Cu
$\epsilon_4$	Crystal cubic anisotropy	0.01	–
$\Gamma$	Gibbs–Thomson coefficient	0.236	$\text{K}\cdot\mu\text{m}$

the scaling growth laws for the copper concentrations considered here [27]. The accuracy of the present algorithm is mainly conditioned by the minimum grid spacing used to mesh the region near the solid–liquid interface [6]. To ensure comparable accuracy for the two concentrations considered (3 and 4 wt% Cu), we use the same interface width,  $W_0 = 1.0 \mu\text{m}$ , which results in the same interface grid size,  $(\Delta x)_{\min} = 0.78 \mu\text{m}$  in both cases. As seen in Equation (5), the capillary length is smaller at higher concentrations. The convergence numerical parameter  $\xi = W_0/d_0$  is thus set to 28.4 and 37.9, respectively. For  $c_0 = 4$  wt% Cu, a convergence test with  $\xi$  showed that variations of a small percentage are expected when  $\xi$  is further decreased. Moreover, for the finite difference algorithm used in BEA, convergence with  $W_0$  was found to be satisfactorily reached for comparable  $\xi$  values [4]. The time step is set to  $0.1\tau_0$ , that is  $5.248 \times 10^{-4}$  s and  $6.998 \times 10^{-4}$  s for  $c_0 = 3$  and 4 wt% Cu, respectively.

The initial value for the preconditioned phase field is  $\psi(\vec{r}) = R_0 - r$ , with  $R_0$  the radius of the spherical solid seed and  $r$  the distance from point  $\vec{r}$  to the seed center. The initial value of

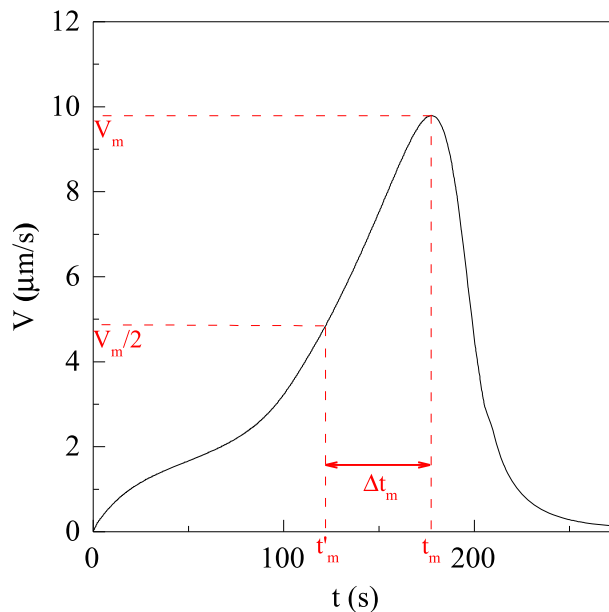


**Figure 2.** Dendrite tip velocity  $V$  as a function of time.  $c_0 = 4.0$  wt% Cu and  $L = 1000$   $\mu\text{m}$ .

the rescaled solute concentration field is  $U(\vec{r}) = 0$ . Mirror (no-flux) conditions are constantly imposed at all the domain boundaries. Thus, it is sufficient to simulate a quarter of the whole sample plane  $xz$ , for instance,  $x \geq 0$  and  $z \geq 0$ . For the same reason, only one half of the sample thickness is necessary, for instance,  $y \geq 0$ . Altogether, we only simulate an eighth of the sample and complete it by applying symmetries; the origin of the numerical domain is thus the center of the solid. Due to the no-flux boundary conditions, mirror dendrites develop and progress toward the reference dendrite from the right and from above, causing dendrite-dendrite collisions after some time. The dimensions  $L \times L \times H$  of the simulated physical domains are the same as in BEA, i.e.,  $L = 800.0, 1000.0, 1200.0$   $\mu\text{m}$  and  $H = 100.0$   $\mu\text{m}$ . They are chosen to reproduce the geometry of recent experiments using thin samples in order to visualize dendritic growth by real-time X-ray imaging [4, 12].

### 3. Growth scaling law

Figure 2 shows a typical curve for the dendrite tip velocity as a function of time that is obtained in our simulations. In BEA, we proposed to characterize such curves by the maximum velocity,  $V = V_m$ , and by the time  $\Delta t_m$  necessary for the tip to accelerate from  $V_m/2$  to  $V_m$  (see Figure 2). It was shown in [4, 11] that this fast growth regime corresponds to a crossover between free growth (before the inflexion point) during which the initial globular nuclei basically develop primary dendritic arms, to early growth during which the interactions between two opposite dendrites develop with the increasing overlap of their diffusion fields (after the inflexion point). The grain morphological evolution from an initial spherical seed to the final coarsened dendrite with developed sidebranches is shown in Figure 3. Owing to the drastic increase of the computing resources needed at the late solidification stage when the secondary arms develop, the simulations are ended before late ripening, as the one shown in BEA, is reached.



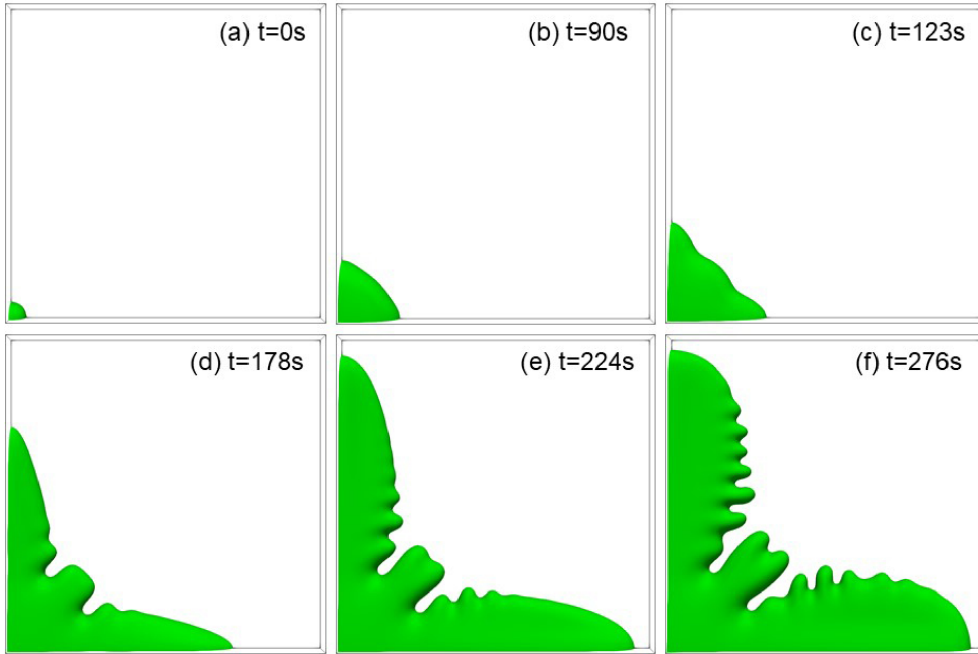


**Figure 3.** Snapshots showing the growth of a dendrite simulated in a thin domain of size  $1000 \times 100 \times 1000 \mu\text{m}^3$  ( $\psi = 0$  isosurfaces are represented). Perspective views are shown to give a better 3D impression: (a) initial condition, (b) slow growth, (c) fast growth, (d) end of the fast growth ( $V = V_m$ ), (e) early ripening, (f) ongoing ripening.  $c_0 = 4.0$  wt% Cu.

The numerical values of  $V_m$  and  $\Delta t_m$  obtained in the present study are shown in Table 2, together with the ones obtained in BEA at lower copper concentrations. For the latter ones, the dimensionless length

$$\Lambda = \frac{L_m}{L} = \frac{V_m \Delta t_m}{L}, \quad (17)$$

was found to be roughly a constant,  $\Lambda = \text{cst}$  [4]. The value  $\Lambda \approx 0.546$  was quoted in BEA but a recent reanalysis of the original data rather gave the value  $\Lambda \approx 0.550$  that will be used hereafter [27].

Figure 4 represents the dimensionless length  $\Lambda$  as a function of the dimensionless variable

$$\sigma = \frac{c_0}{c_0^*} + \frac{L - L^*}{L^*}. \quad (18)$$

This variable expresses both the concentration dependence of  $\Lambda$  through the ratio  $c_0/c_0^*$  and its domain size dependence through the group  $L/L^* - 1$ , where  $c_0^*$  and  $L^*$  are two reference quantities that are respectively taken equal to 1 wt% Cu and 1000.0  $\mu\text{m}$  here. In Figure 4, the  $\Lambda$  data are grouped by triplets corresponding to a given value of  $c_0$  and increasing values of  $L$ . Concerning the evolution of  $\Lambda$  with  $L$ , one obtains different behaviors for the different triplets (globally increasing, globally decreasing, strongly nonuniform). This suggests that, on average,  $\Lambda$  does not vary significantly with  $L$ , as already remarked in BEA. Concerning the evolution of  $\Lambda$  with  $c_0$ , if each triplet is replaced by a single point placed at the triplet average coordinates, one again observes no obvious dependence on  $c_0$ . Thus, it is a very good approximation to consider that  $\Lambda$  is roughly equal to a dimensionless constant, as in BEA. A simple average of the  $\Lambda$  estimates obtained for all the concentrations and all the system sizes roughly gives 0.539, which is very close

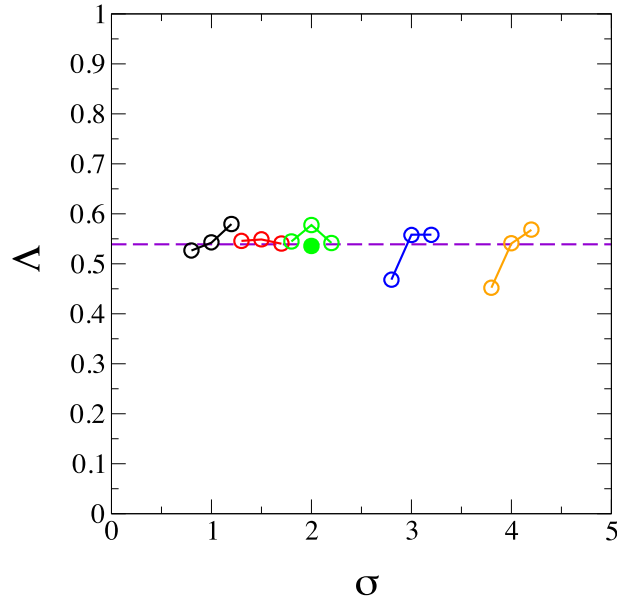


**Figure 4.** Dimensionless growth length  $\Lambda = L_m/L$  as a function of the dimensionless variable  $\sigma = (c_0/c_0^*) + (L - L^*/L^*)$  ( $c_0^* = 1$  wt% Cu and  $L^* = 1000.0$   $\mu\text{m}$ ). Each color corresponds to a triplet of data obtained at a given  $c_0$  and for increasing values of  $L$ . The filled circle results from a simulation using the present parallel adaptive code for  $c_0 = 2$  wt% Cu and  $L = 1000.0$   $\mu\text{m}$  and the empty circle just above is the corresponding result found in BEA with a finite difference code.

**Table 2.** Numerical estimates of  $V_m(c_0, L)$ , and  $\Delta t_m(c_0, L)$  obtained in BEA and in the present study at different copper concentrations  $c_0$  and for different numerical domain length  $L$ . Also given is the growth length  $\Delta x_m$  defined later in Equation (20).

	$c_0$ (wt% Cu)	$L$ ( $\mu\text{m}$ )	$V_m$ ( $\mu\text{m/s}$ )	$\Delta t_m$ (s)	$\Delta x_m$ ( $\mu\text{m}$ )	
BEA	1.0	800.0	16.52	25.50	303.00	
		1000.0	25.74	21.09	397.00	
		1200.0	33.12	21.00	540.00	
	1.5	800.0	12.13	36.00	327.00	
		1000.0	20.38	26.94	410.00	
		1200.0	31.14	20.83	473.00	
	2.0	800.0	9.610	45.35	333.00	
		1000.0	15.67	36.86	432.00	
		1200.0	24.77	26.24	504.00	
Present	2.0	1000.0	16.63	32.21	415.00	
		3.0	800.0	7.440	50.35	293.56
			1000.0	12.18	45.79	443.75
	1200.0		18.90	35.42	522.60	
	4.0	800.0	6.010	60.18	286.07	
		1000.0	9.790	55.28	416.69	
		1200.0	15.00	45.48	514.67	

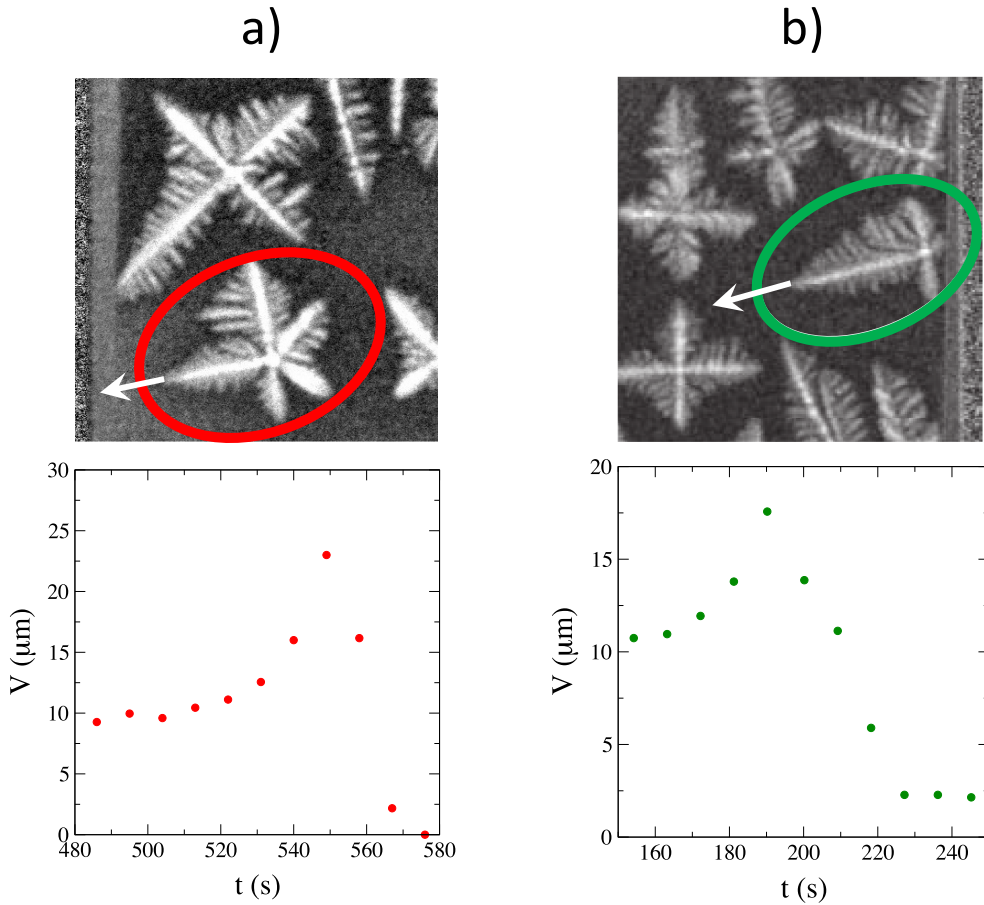


**Figure 5.** Two experimental examples of dendritic interactive growth in Al-4 wt% Cu samples (top row). The sample sections represented are both  $3 \times 3 \text{ mm}^2$  in size. The reference dendrites are encircled and, in each case, an arrow indicates the growth direction of the dendrite tip that is observed. The corresponding tip growth velocities are represented as functions of time (bottom row): (a) adapted from Ref. [4], and (b) adapted from Ref. [11].

to the value 0.550 obtained for the lower copper concentrations  $c_0$ . This result definitely confirms the scaling law

$$\Lambda = cst \approx 0.539. \quad (19)$$

It is to be noted that the initial condition imposed to the concentration field  $U$  in the present work ( $U = 0$ ) differs from the one imposed in BEA (solid-liquid equilibrium condition). Our results thus confirm that no significant influence of the initial condition can be detected, as it was already the case in reference [27].

As illustrated in Figure 5, direct comparison with experiments at 4 wt% Cu is possible for a few cases that have been recently described in the literature [4, 11]. In these experimental situations, little gravity effects are expected. The experimental results for the dimensionless length  $\Lambda$  are reported in Table 3. In this table, the first entry corresponds to the situation shown in Figure 5a: this case is very comparable to the present simulations because a single dendrite arm grows toward the crucible boundary. The second table entry corresponds to a more complicated situation shown in Figure 5b: several dendrites simultaneously grow toward each other. The free

**Table 3.** Dimensionless ratio  $\Lambda = (V_m \Delta t_m)/L$  estimated from two experiments at copper concentration  $c_0 = 4.0$  wt% Cu.

Ref.	$\Lambda$
[4]	0.549
[11]	0.533–0.648

distance ahead of the reference dendrite (that is encircled in the figure), may be taken with respect to the cross-shaped dendrite that sits in the bottom left corner of the figure or to the elongated slanted dendrite that grows from below in between them. These two choices explain the interval reported in the last entry of Table 3. In both cases, the experimental results are in good agreement with the estimate  $\Lambda \simeq 0.539$  predicted by the present study.

#### 4. Physical justification of the scaling law for the growth length

The main result of the previous section is that the dimensionless growth length  $\Lambda$  remains constant when  $c_0$  and  $L$  vary in an extended range of values. A simple justification of this result can be provided by simple considerations, some of which were already mentioned in BEA. To proceed, it is useful to switch to a simple physical quantity related to the dendrite tip position,  $x_{\text{tip}}(t)$ . An alternative growth length is obtained by integrating the tip velocity,  $V(t)$  over a given time interval. We consider again the time interval  $[t'_m, t_m]$  during which the tip velocity increases from  $V_m/2$  to  $V_m$ . The corresponding growth length,

$$\Delta x_m = \int_{t'_m}^{t_m} V(t) dt = x_{\text{tip}}(t_m) - x_{\text{tip}}(t'_m), \quad (20)$$

corresponds to the growth of the dendrite tip during the crossover regime already discussed in the previous section. Figure 6 shows the time evolution of  $x_{\text{tip}}$  for a given copper concentration and three different values of the domain length  $L$ . It is obvious from this figure that the three curves can be rescaled to a common master curve by rescaling the time (see below) and rescaling the tip position by  $L$ . The natural scaling variable for the tip position is thus  $x_{\text{tip}}/L$ , so we expect that the scaled alternative growth length

$$\chi = \Delta x_m / L \quad (21)$$

is a constant. One can object that, instead of  $x_{\text{tip}}/L$ , a better choice for the scaling variable would be  $(x_{\text{tip}} - R_0)/(L - R_0)$ , where  $R_0$  is the radius of the initial solid nucleus. Although this choice is more rigorous, it would not modify  $\chi$  by much because  $L$  is always much larger than  $R_0$  here.

We now return to BEA, where it was shown that a universal law relates the scaled velocity

$$Y = (2V - V_m)/V_m \quad (22)$$

to the scaled time

$$X = (t - t'_m)/\Delta t_m, \quad (23)$$

with  $\Delta t_m = t_m - t'_m$ . For these scaled coordinates one obtained a universal curve  $Y(X)$  that could be parametrized by a fourth-order polynomial,  $Y = A_1 X + A_2 X^2 + A_3 X^3 - A_4 X^4$ . The four prefactors  $A_{1-4}$  were obtained by a numerical fit to the data points. The area  $\mathcal{A}$  below the universal curve  $Y(X)$  is given by

$$\mathcal{A} = \int_0^1 Y dX = \frac{2}{L_m} \int_{t'_m}^{t_m} V(t) dt - 1 = \frac{2}{L_m} \Delta x_m - 1, \quad (24)$$

with  $L_m = V_m \Delta t_m$ . Using (21), one finally sees that

$$\Lambda = \frac{L_m}{L} = \frac{2\chi}{\mathcal{A} + 1}. \quad (25)$$

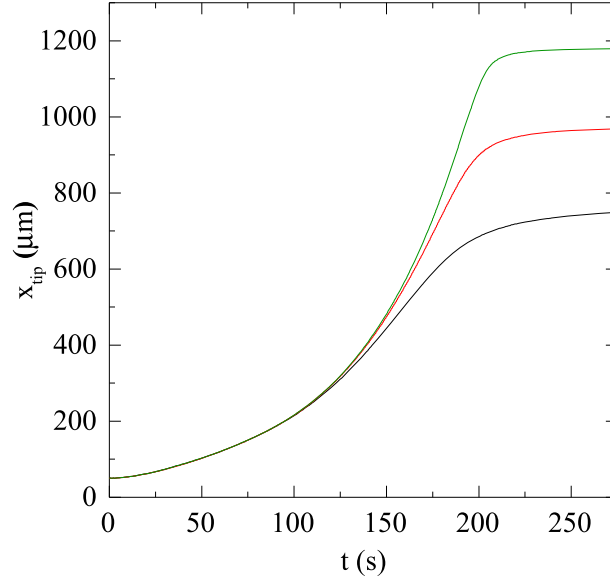


**Figure 6.** Tip position  $x_{\text{tip}}$  as a function of time  $t$ . Increasing curves correspond to increasing values of  $L$  (800.0, 1000.0, 1200.0  $\mu\text{m}$ ).  $c_0 = 4.0$  wt% Cu.

This is indeed equivalent to the scaling relation  $\Lambda = \text{cst}$ , provided that our physical argument that  $\chi$  is a constant is justified. Figure 7 shows our simulation data for  $\chi$  versus  $\sigma$ . They do confirm with a good accuracy that  $\chi$  is a constant  $\approx 0.411$ . Using the  $A_{1-4}$  coefficients obtained in BEA, one can estimate that the area  $\mathcal{A} \approx 0.5057$ . Combining both results, one finally obtains

$$\Lambda = \frac{2\chi}{\mathcal{A} + 1} \approx 0.546, \quad (26)$$

a value that is very close to the estimate 0.539 obtained in the previous section. To summarize this section, the scaling law  $\Lambda = \text{cst}$  can be shown to result from a simple physical scaling argument,  $\Delta x_m / L = \text{cst}$ , relating the growth length  $\Delta x_m$  during the crossover regime to the total available free growth distance  $L$ .

## 5. Summary and conclusion

In summary, the scaling law  $\Lambda = \text{cst}$  predicted in BEA has been tested for the dimensionless length  $\Lambda = L_m / L$ , where  $L_m = V_m \Delta t_m$  is a length related to the increase of the dendrite tip velocity in the fast growth regime, and  $L$  is half the average distance between dendritic nuclei, related to the volume density of the nuclei in the sample. New simulation results have been obtained at higher copper concentrations that are used in industrial applications. This has been made possible by using a parallel adaptive finite element algorithm. A careful analysis of the data has confirmed that, within numerical errors,  $\Lambda$  is indeed a constant, thus confirming that it shows no concentration and no dendrite density dependence. Physical arguments have been developed to justify this scaling law.

A few remarks can be formulated in conclusion. The addition of thermodynamic effects, like thermal fluctuations or concentration dependence of the phase diagram, was recently considered [27]. There again, the scaling laws predicted in BEA were found to be very robust against these effects. The combination of these results with the ones of the present study thus conveys an impression of great robustness for the proposed scaling relation. Confinement effects are necessarily present for the thin experimental samples considered here through numerical simulations.

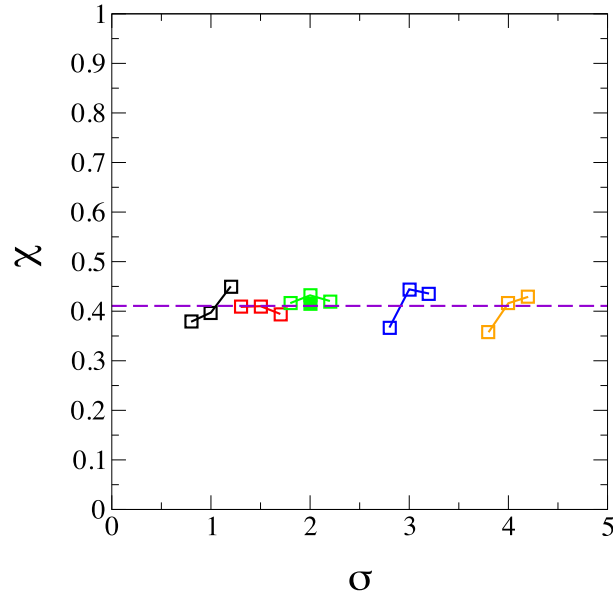


**Figure 7.** Dimensionless alternative growth length  $\chi = \Delta x_m / L$  as a function of the dimensionless variable  $\sigma = (c_0 / c_0^*) + (L - L^* / L^*)$  ( $c_0^* = 1$  wt% Cu and  $L^* = 1000.0$   $\mu\text{m}$ ). Each color corresponds to a triplet of data obtained at a given  $c_0$  and for increasing values of  $L$ . The filled square results from a simulation using the present parallel adaptive code for  $c_0 = 2$  wt% Cu and  $L = 1000.0$   $\mu\text{m}$  and the empty square slightly above is the corresponding result found in BEA with a finite difference code.

Quantifying these effects would be important to generalize the present results to a wider class of experimental situations corresponding to different confinement levels. As discussed above, in the experimental studies of equiaxed solidification the situation generally differ from the simplified geometry assumed in the present simulations. The main differences are that more than two dendrites simultaneously interact, their respective orientations are not correlated, and their relative separation distances vary from one experimental case to the other. It would be interesting in the future to test dendritic interactions in a more statistical way by performing simulations at larger scales and by analyzing a sufficiently large number of different cases. In a wider context, it would be very instructive to test the possibility to extend the present scaling laws to other alloys. Indeed, the growth dynamics may substantially depend on materials characteristics as surface energy anisotropies that can vary either in strength or in crystal symmetries (or both). Recent results obtained for AlGe alloys that, in addition to the four-fold anisotropy of Al–Cu, also display a six-fold anisotropy show that this alloy would probably be a good candidate to conduct such tests [28, 29]. The present phase-field code models solidification of Al–Cu in purely diffusive conditions. In ground experiments this is very seldom the case because gravity may induce convection in the liquid, solute accumulation at the sample bottom, and grain buoyancy or grain sedimentation [30]. To compare simulations to experiments, two approaches are thus possible: either perform experiments in microgravity conditions or refine the phase-field models to include gravity effects. Both approaches are currently explored.

### Conflicts of interest

Authors have no conflict of interest to declare.

## Acknowledgments

We would like to thank CNES. This work was supported by the Youth Innovation Promotion Association CAS, and China Postdoctoral Science Foundation (Grant No. 2021TQ0335).

## References

- [1] S. S. Miller, L. Zhuang, J. Bottema, A. J. Wittebrood, P. De Smet, A. Haszlar, A. Viregge, "Recent development in aluminium alloys for the automotive industry", *Mater. Sci. Eng. A* **280** (2000), p. 37-49.
- [2] J. G. Kaufman, E. L. Rooy, *Aluminum Alloy Castings: Properties, Processes and Applications*, AMS International, Materials Park, OH, 2004.
- [3] L. F. Mondolfo, *Aluminum Alloys: Structure and Properties*, Butterworths, London, 1976, 693-758 pages.
- [4] A. K. Boukellal, J.-M. Debierre, G. Reinhart, H. Nguyen-Thi, "Scaling laws governing the growth and interaction of equiaxed Al-Cu dendrites: A study combining experiments with phase-field simulations", *Materialia* **1** (2018), p. 62-69.
- [5] P. Pelcé, *New Visions on Form and Growth: Fingered Growth, Dendrites, and Flames*, Oxford University Press, New York, 2004.
- [6] T. Z. Gong, Y. Chen, Y. F. Cao, X. H. Kang, D. Z. Li, "Fast simulations of a large number of crystals growth in centimeter-scale during alloy solidification via nonlinearly preconditioned quantitative phase-field formula", *Comput. Mater. Sci.* **147** (2018), p. 338-352.
- [7] A. Badillo, C. Beckermann, "Phase-field simulation of the columnar-to-equiaxed transition in alloy solidification", *Acta Mater.* **54** (2006), p. 2015-2026.
- [8] G. Boussinot, M. Apel, "Phase field and analytical study of mushy zone solidification in a static thermal gradient: From dendrites to planar front", *Acta Mater.* **122** (2017), p. 310-321.
- [9] A. J. Clarke, D. Turret, S. D. Imhoff, P. J. Gibbs, K. Fezzaa, A. Karma, "Microstructure selection in thin-sample directional solidification of an Al-Cu alloy: In situ X-ray imaging and phase-field simulations", *Acta Mater.* **129** (2017), p. 203-216.
- [10] F. Li, W. Zhi-Ping, Z. Chang-Sheng, L. Yang, "Phase-field model of isothermal solidification with multiple grain growth", *Chin. Phys. B* **18** (2009), p. 1985-1991.
- [11] Y. Chen, D. Z. Li, B. Billia, H. Nguyen-Thi, X. B. Qi, N. M. Xiao, "Quantitative phase-field simulation of dendritic equiaxed growth and comparison with in situ observation on Al-4 wt.% Cu alloy by means of synchrotron X-ray radiography", *ISIJ Int.* **54** (2014), p. 445-451.
- [12] A. Bogno, H. Nguyen-Thi, G. Reinhart, B. Billia, J. Baruchel, "Growth and interaction of dendritic equiaxed grains: In situ characterization by synchrotron X-ray radiography", *Acta Mater.* **61** (2013), p. 1303-1315.
- [13] K. Glasner, "Nonlinear preconditioning for diffuse interfaces", *J. Comput. Phys.* **174** (2001), p. 695-711.
- [14] J.-M. Debierre, R. Guérin, K. Kassner, "Crystal growth in a channel: Pulsating fingers, merry-go-round patterns, and seesaw dynamics", *Phys. Rev. E* **88** (2013), article no. 042407.
- [15] N. Bergeon, D. Turret, L. Chen, J.-M. Debierre, R. Guérin, R. Ramirez, B. Billia, A. Karma, R. Trivedi, "Spatiotemporal dynamics of oscillatory cellular patterns in three-dimensional directional solidification", *Phys. Rev. Lett.* **110** (2013), article no. 226102.
- [16] J. Ghmadh, J.-M. Debierre, J. Deschamps, M. Georgelin, R. Guérin, A. Pocheau, "Directional solidification of inclined structures in thin samples", *Acta Mater.* **74** (2014), p. 255-267.
- [17] A. K. Boukellal, A. K. Sidi Elvalli, J.-M. Debierre, "Equilibrium and growth faceted shapes in isothermal solidification of silicon: 3D phase-field simulations", *J. Cryst. Growth* **522** (2019), p. 37-44.
- [18] A. Karma, "Phase-field formulation for quantitative modeling of alloy solidification", *Phys. Rev. Lett.* **87** (2001), article no. 115701.
- [19] B. Echebarria, R. Folch, A. Karma, M. Plapp, "Quantitative phase-field model of alloy solidification", *Phys. Rev. E* **70** (2004), article no. 061604.
- [20] A. Karma, W. J. Rappel, "Quantitative phase-field modeling of dendritic growth in two and three dimensions", *Phys. Rev. E* **57** (1998), p. 4323-4349.
- [21] J. J. Hoyt, M. Asta, A. Karma, "Method for computing the anisotropy of the solid-liquid interfacial free energy", *Phys. Rev. Lett.* **86** (2001), p. 5530-5533.
- [22] W. Bangerth, D. Davydov, T. Heister, L. Heltai, G. Kanschat, M. Kronbichler, M. Maier, B. Turcksin, D. Wells, "The deal.II Library, Version 8.4", *J. Numer. Math.* **24** (2016), p. 135-141.
- [23] W. Bangerth, "Reference document for deal.II" (2016-03-15), <https://www.dealii.org/developer/doxygen/deal.II/Tutorial.html>.
- [24] M. Kronbichler, W. Bangerth, "The step-22 tutorial program" (2022-06-23), [https://www.dealii.org/current/doxygen/deal.II/step\\_22.html#Results](https://www.dealii.org/current/doxygen/deal.II/step_22.html#Results).

- [25] R. Hultgren, P. R. Desai, D. T. Hawkins, M. Gleiser, K. K. Kelley, *Selected Values of the Thermodynamic Properties of Binary Alloys*, American Society for Metals, Metals Park, OH, 1973, 151-153 pages.
- [26] H. Okamoto, *Phase Diagrams for Binary Alloys*, 2nd ed., ASM International, Materials Park, OH, 2010.
- [27] A. K. Boukellal, M. Rouby, J.-M. Debierre, "Tip dynamics for equiaxed Al-Cu dendrites in thin samples: Phase-field study of thermodynamic effects", *Comput. Mater. Sci.* **186** (2021), article no. 110051.
- [28] M. Becker, S. Klein, F. Kargl, "Free dendritic tip growth velocities measured in Al-Ge", *Phys. Rev. Mater.* **2** (2018), article no. 073405.
- [29] M. Becker, L. Sturz, D. Bräuer, F. Kargl, "A comparative in situ X-radiography and DNN model study of solidification characteristics of an equiaxed dendritic Al-Ge alloy sample", *Acta Mater.* **201** (2020), p. 286-302.
- [30] H. Nguyen-Thi, A. Bogno, G. Reinhart, B. Billia, R. H. Mathiesen, G. Zimmermann, Y. Houltz, K. Löth, D. Voss, A. Verga, F. de Pascale, "Investigation of gravity effects on solidification of binary alloys with in situ X-ray radiography on earth and in microgravity environment", *J. Phys. Conf. Ser.* **327** (2011), article no. 012012.